RESEARCH ARTICLE

Key Points:
- The low-energy ion fluxes were enhanced dramatically in both the parallel and perpendicular directions after the shock arrivals
- The rapid response of low-energy ions is due to drifts of plasmaspheric population by the enhanced electric field
- Ion outflows contribute to the enhanced parallel population that last longer than the perpendicular population

Rapid enhancement of low-energy (<100 eV) ion flux in response to interplanetary shocks based on two Van Allen Probes case studies: Implications for source regions and heating mechanisms

Chao Yue[1,2], Wen Li[1], Yukitoshi Nishimura[1], Qiugang Zong[3], Qianli Ma[1], Jacob Bortnik[1], Richard M. Thorne[1], Geoffrey D. Reeves[4,5], Harlan E. Spence[6], Craig A. Kletzing[7], John R. Wygant[8], and Michael J. Nicolls[9]

[1]Department of Atmospheric and Oceanic Sciences, UCLA, Los Angeles, California, USA, [2]University Corporation for Atmospheric Research, Boulder, Colorado, USA, [3]Institute of Space Physics and Applied Technology, Peking University, Beijing, China, [4]Space Science and Applications Group, Los Alamos National Laboratory, Los Alamos, New Mexico, USA, [5]Space Sciences Division, New Mexico Consortium, Los Alamos, New Mexico, USA, [6]Institute for the Study of Earth, Oceans, and Space, University of New Hampshire, Durham, New Hampshire, USA, [7]Department of Physics and Astronomy, University of Iowa, Iowa City, Iowa, USA, [8]School of Physics and Astronomy, University of Minnesota, Minneapolis, Minnesota, USA, [9]SRI International, Menlo Park, California, USA

Abstract Interactions between interplanetary (IP) shocks and the Earth's magnetosphere manifest many important space physics phenomena including low-energy ion flux enhancements and particle acceleration. In order to investigate the mechanisms driving shock-induced enhancement of low-energy ion flux, we have examined two IP shock events that occurred when the Van Allen Probes were located near the equator while ionospheric and ground observations were available around the spacecraft footprints. We have found that, associated with the shock arrival, electromagnetic fields intensified, and low-energy ion fluxes, including H^+, He^+, and O^+, were enhanced dramatically in both the parallel and perpendicular directions. During the 2 October 2013 shock event, both parallel and perpendicular flux enhancements lasted more than 20 min with larger fluxes observed in the perpendicular direction. In contrast, for the 15 March 2013 shock event, the low-energy perpendicular ion fluxes increased only in the first 5 min during an impulse of electric field, while the parallel flux enhancement lasted more than 30 min. In addition, ionospheric outflows were observed after shock arrivals. From a simple particle motion calculation, we found that the rapid response of low-energy ions is due to drifts of plasmaspheric population by the enhanced electric field. However, the fast acceleration in the perpendicular direction cannot solely be explained by $\mathbf{E} \times \mathbf{B}$ drift but betatron acceleration also plays a role. Adiabatic acceleration may also explain the fast response of the enhanced parallel ion fluxes, while ion outflows may contribute to the enhanced parallel fluxes that last longer than the perpendicular fluxes.

1. Introduction

The electromagnetic fields and energetic particles in geospace can be strongly affected by impacts of interplanetary (IP) shocks on the Earth's magnetosphere. The interaction between IP shocks and the Earth's magnetosphere has been extensively studied in many aspects, such as responses to IP shocks at the geosynchronous orbit [e.g., *Thomsen et al.*, 1998; *Li et al.*, 2003; *Wang et al.*, 2009; *Yue et al.*, 2009, 2011a], plasma sheet [*Yue et al.*, 2013], and on the ground [e.g., *Zhou and Tsurutani*, 2001; *Liou et al.*, 2003; *Yue et al.*, 2010; *Yue and Zong*, 2011b], as well as the IP shock-induced ULF wave impacts on plasma pitch angle scattering and accelerations [*Zong et al.*, 2009, 2011, 2012; *Foster et al.*, 2015].

However, there are few studies focusing on the shock-related low-energy (<100 eV) particle enhancement and their source regions. Although cold ions are typically invisible to instruments during quiet periods, their presence can have a significant role. For example, cold ions can be transported and heated to form the hotter ion populations that contribute to the ring current [e.g., *Keika et al.*, 2013], the presence of cold ions may affect the dayside reconnection rate [e.g., *André and Cully*, 2012], and cold ion composition is also related to electromagnetic ion cyclotron (EMIC) wave growth [e.g., *Keika et al.*, 2013]. *Zhang et al.* [2012] have used five Time History of Events and Macroscale Interactions during Substorms (THEMIS) spacecraft that were located at different regions to examine the global magnetospheric response to an IP shock that occurred

on 28 May 2008. They found that the plasmaspheric plume density rapidly increased by about an order of magnitude in 4 min after the shock arrival and the ion distribution changed from isotropic to strongly aniso-tropic, which is favorable for exciting EMIC waves observed by THEMIS A. In addition, the low-energy ion flux was found to increase when there existed a substantial flow caused by the impact of the IP shock, and they concluded that the ions were accelerated from the cold plasmaspheric plume population. *Zong et al.* [2012] investigated the response of the inner magnetospheric H^+ and O^+ ions to a strong IP shock. They found that the ion energy spectra from 10 eV to ~40 keV were highly correlated with the cross product of observed ULF wave electric and magnetic fields. They further demonstrated that the ion acceleration due to the IP shock compression on the Earth's magnetic field caused by the adiabatic effect was insufficient to explain the observation, and the major contribution came from the electric field carried by ULF waves via drift-bounce resonance.

Although the plasmaspheric origin has been a primary focus of the past studies, the ionosphere can be another source of enhanced low-energy plasma. Previous studies [e.g., *André and Yau*, 1997; *Fuselier et al.*, 2001] have demonstrated that energetic particle precipitation deposits energy at lower altitudes where the plasma is dominated by collisions [*Gombosi and Killeen*, 1987], and it takes some time (>20 min) to affect the topside ionosphere with direct auroral energy input. In contrast, low-energy particle precipitation depos-its considerable energy into higher altitudes, such as the topside of the *F* region and even up to the exobase (~350–1000 km) [*Fuselier et al.*, 2001]. This may lead to a more rapid outflow response. The ambipolar electric field could be enhanced, and ionospheric scale heights could be raised because of the high-altitude energy deposition, resulting in the accelerated light ion outflows [e.g., *Horwitz and Moore*, 1997]. In addition, fast aur-oral plasma wind heats heavy ions strongly, increasing scale heights sufficiently for heavy ions to escape the Earth's gravity [*Heelis et al.*, 1993]. This scale height increase could result in a rapid escape of ions from the ionosphere.

Zong et al. [2012] and *Zhang et al.* [2012] have suggested that the $\mathbf{E} \times \mathbf{B}$ drift is responsible for low-energy ion flux enhancements. However, from our investigation, the low-energy ion acceleration cannot be fully explained by the $\mathbf{E} \times \mathbf{B}$ drift, and additional acceleration mechanisms are needed. In this paper, we use the Van Allen Probes and conjugate ionospheric and ground-based observations to address possible source and acceleration mechanisms of the energized low-energy particles in both perpendicular and parallel direc-tions due to the impact of IP shocks. The paper will be organized as following. In section 2, we briefly describe particle and field measurements used in this study and the theories of particle adiabatic accelerations. The detailed observational responses to two typical IP shock cases are presented in section 3. Section 4 discusses and summarizes our main findings.

2. Methodology and Instrumentation

We present two IP shock events (on 2 October 2013 and 15 March 2013) observed by Van Allen Probe B when it was located near the magnetic equator with relatively good coverage of ionospheric and ground observa-tions. The other Van Allen Probe A was too close to the Earth to provide additional useful information. We identified IP shocks using OMNI data as abrupt increases in the solar wind dynamic pressure and *SYM-H* index [*Iyemori*, 1990; *Iyemori and Rao*, 1996], whose stepwise jumps can be used as indicators of magnetospheric compression [*Liou et al.*, 2003; *Keika et al.*, 2008]. The Van Allen Probes (Radiation Belt Storm Probes (RBSP)) mission with two identically instrumented spacecraft (probes A and B) was launched into near-equatorial orbit (10° inclination) on 30 August 2012. They have an orbital period of ~9 h, a perigee at ~1.1 R_E, and an apogee at ~5.8 R_E [*Mauk et al.*, 2013]. Both satellites are equipped with comprehensive suites of particle and field measurement instrumentation. In this paper, we use the particle measurements from the Helium, Oxygen, Proton, and Electron (HOPE) Mass Spectrometer [*Funsten et al.*, 2013] of the Energetic particle, Composition, and Thermal plasma (ECT) Suite [*Spence et al.*, 2013] and the field measurements from the Electric Field and Waves (EFW) instrument [*Wygant et al.*, 2013]. The HOPE instrument measures the distribu-tions of ions, including proton (H^+), helium (He^+), and oxygen (O^+), over the energy range from ~1 eV to 50 keV and electrons (e^-) from ~15 eV to 50 keV by using a combination of an electrostatic analyzer and a time-of-flight measurement. The magnetometer of the Electric and Magnetic Field Instrument Suite and Integrated Science (EMFISIS) [*Kletzing et al.*, 2013] measures the DC magnetic field and magnetic fluctuations up to 30 Hz. The EFW instrument measures spin-plane components of the electric field. It should be noted

that the EFW instrument onboard Van Allen Probes only provided y and z components of electric field in a modified Geocentric Solar Elliptic coordinate, and the E_x component in this study was derived by assuming $\mathbf{E} \times \mathbf{B} = 0$. In addition, the low-altitude DMSP satellites, ground-based Poker Flat Advanced Modular Incoherent Scatter Radar (PFISR), and THEMIS All-Sky Imager (ASI) [Mende et al., 2008] are also used in this study. DMSP are Sun-synchronous satellites in nearly circular polar orbits at an altitude of roughly 840 km and a period of approximately 101 min. Here we have used the particle data obtained from the Special Sensor for Precipitating Particles, version 4 (SSJ4) instrument, which measures ions and electrons from ~30 eV to 30 keV [Hardy et al., 1984] and the vertical and cross-track horizontal drift velocity from the Driftmeter [Heelis, 2006].

It is well known that the induced electric field in response to the passage of IP shock could shift the plasma distribution function to higher energies in the perpendicular direction due to the $\mathbf{E} \times \mathbf{B}$ drift, and thus, hidden cold plasma (plasma at energies below minimum energy threshold of the instrument) can be measured within the particle detector energy range. The final energy of the plasma would be

$$W_{\perp,f} = \frac{1}{2} m_i \left(\frac{|\mathbf{E} \times \mathbf{B}|}{B^2} \right)^2 + W_{\perp,i} \tag{1}$$

Here $W_\perp$ is the total perpendicular energy, $\mathbf{E}$ and $\mathbf{B}$ are electric and magnetic fields, m_i is the ion mass. The subscripts "i" and "f" represent the initial and final states, respectively.

If the particles observed by the spacecraft were not localized, i.e., the observed particles drift from other locations, they would also experience betatron acceleration or deceleration depending on satellite location and particle drift direction. In this situation, the energy gain due to betatron acceleration can be expressed as the following equation:

$$W_{\perp,f} = W_{\perp,i} \frac{B_f(L = L_f)}{B_i(L = L_i)} \tag{2}$$

The subscripts i and f represent the initial and final states, respectively. Here $L_i = L_f + \int v_r dt$ is the back-traced particle trajectory in the radial direction and v_r is the particle radial velocity in a local field-aligned coordinate system. Considering an IP shock impact, B_i is the magnetic field intensity without the impact of IP shock at $L = L_i$ and B_f is the magnetic field intensity affected by the IP shock impact at satellite location $L = L_f$. In this study, we have used the dipole magnetic field model to represent the quiet time magnetic field configuration and obtain B_i while B_f is the observed magnetic field by Van Allen Probe B. $W_{\perp,i}$ is the initial particle perpendicular energy.

For the particle acceleration in the parallel direction due to the impact of IP shocks, Olson and Lee [1983] performed a study to estimate the magnetic field compressions associated with sudden impulses and have shown that the plasma average energy in the parallel direction is proportional to the power of local magnetic field strength if the first and second adiabatic invariants are conserved:

$$\frac{W_{\|,f}}{W_{\|,i}} = \left(\frac{B_f}{B_i} \right)^a \tag{3}$$

Here $W_\|$ and B are parallel energy and magnetic field intensity, the label i indicates the initial state, before the impinging of the sudden impulse, and α is a constant with its value depending on the field geometry. Previous studies have shown that α varies from 2/3 to 2.5/3 [e.g., Southwood and Kivelson, 1975]. Since the second adiabatic invariant may not be conserved during an IP shock impact, this is just used for estimating parallel acceleration by adiabatic effects.

3. Results

Figure 1 shows the trajectories of Van Allen Probe B for case 1 from 01:25 UT to 02:25 UT on 2 October 2013 (in black color) and for case 2 from 04:55 UT to 05:55 UT on 15 March 2013 (in red color) in the x-y plane (Figure 1a) and x-z plane (Figure 1b) in the geocentric solar magnetospheric (GSM) coordinates. The spacecraft was in the post noon sector in case 1 and around midnight in case 2. The two events observed on the dayside and nightside illustrate day-night similarities and differences in IP shock effects on the inner magnetosphere, especially on those low-energy ions. The black and red curves mark the magnetopause locations
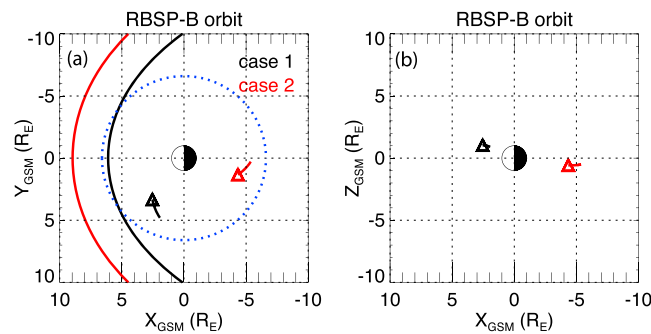
Figure 1. Van Allen Probe B 1 h trajectory projection on the (a) *x-y* plane and (b) *x-z* plane for case 1 (2 October 2013 shock event) in black color and case 2 (15 March 2013 shock event) in red color 30 min prior to and after the IP shock arrival. The triangles mark the position of satellites 30 min prior to the shock arrival. The solid black and red curves are the magnetopause locations in cases 1 and 2, respectively, using the empirical magnetopause model by *Shue et al.* [1998]. The blue dotted circle in Figure 1a is the geosynchronous orbit.

calculated using the model by *Shue et al.* [1998] at the time when the shocks impinge on the Earth's dayside magnetosphere. As shown in the first case, the strong dayside compression caused by the IP shock pushed the dayside magnetopause inside the geosynchronous orbit (the blue dashed circle), while the magnetopause was at around 9 R_E at the subsolar point in the second case when the shock arrived. Although the direct observational evidence of magnetopause crossing at the geosynchronous orbit in the first case was not clear at the shock arrival time due to the GEOS and Los Alamos Nationa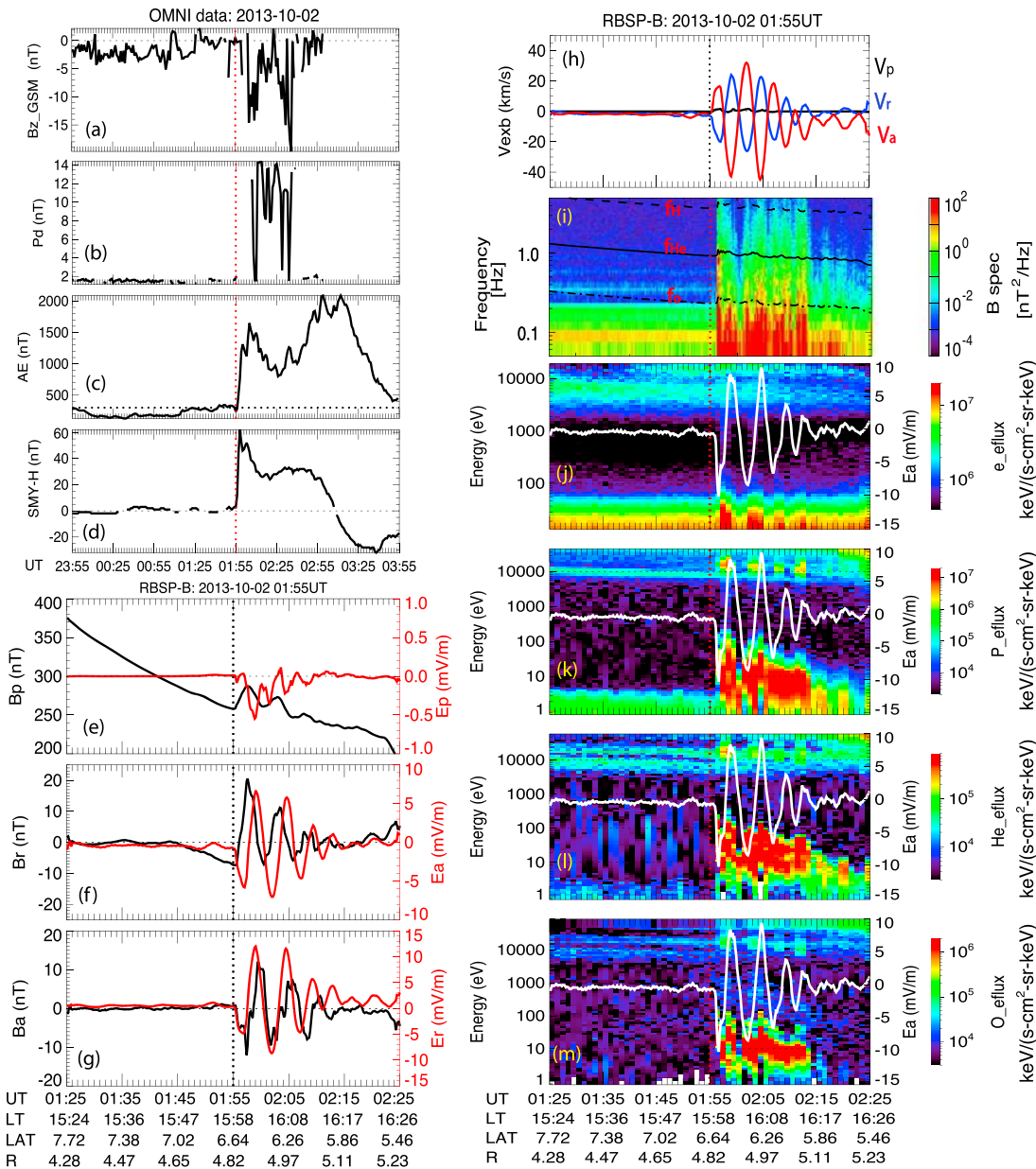l Laboratory (LANL)-GEO satellite orbit limitation, we indeed found that there was magnetopause crossing at the later time around 04:40 UT on 2 October 2013 when LANL-GEO satellite was near the local noon. By comparing the upstream solar wind conditions from THEMIS B observation, the compressional effect was stronger around 01:55 UT than that occurred around 04:40 UT, which supported the magnetopause crossing at the geosynchronous orbit in the first case.

3.1. 2 October 2013 Shock Event

Figures 2a–2d show a summary plot of the solar wind parameters and geomagnetic indices obtained from the OMNI database 1 h prior to and 1 h after the shock arrival. Figures 2e–2m display electromagnetic fields, electric drift velocities, wave magnetic field power spectrogram, and energy fluxes of different particle species measured by Van Allen Probe B within 30 min of the shock arrival time. After the shock arrival, the interplanetary magnetic field (IMF) B_z (Figure 2a) dramatically dropped from 0 to about −14 nT and then fluctuated in the negative range. The solar wind dynamic pressure (Figure 2b) increased from 2 to 14 nPa, compressing the Earth's magnetopause to a location inside of geosynchronous orbit. Meanwhile, the *AE* index (Figure 2c) increased from 300 nT to ~1500 nT, indicating a strong injection around midnight after the shock arrival, which was also observed (not shown) by THEMIS A and E located at around 9 R_E. In addition, the *SYM-H* index (Figure 2d) abruptly jumped from about 0 to 60 nT, which was a typical shock-related signature of sudden commencement associated with the dayside Chapman-Ferraro current.

The electromagnetic fields from Van Allen Probe B observations and the **E** × **B** drift velocity in a local mean field-aligned coordinate system are shown in Figures 2e–2h, where the parallel direction **p** is determined from a 20 min sliding averaged magnetic field, the azimuthal direction **a** is parallel to the cross product of the **p** and the spacecraft position vector, and the **r** component completes the triad. After the shock arrival shown in Figures 2e–2g, the magnetic field was compressed and the electric field was intensified with a maximum amplitude of ~15 mV/m and modulated at the same time by the ULF waves, which were triggered by the sudden compression of the magnetospheric plasma, with a period about 5 min. The dominant component of the **E** × **B** drift was in the azimuthal directions with a magnitude close to 40 km/s (Figure 2h).

Previous studies have shown that the interaction between IP shocks and the Earth's magnetosphere would trigger various types of waves, such as fast magnetosonic waves [e.g., *Kepko and Spence*, 2003], whistler mode waves [*Parks*, 1975; *Fu et al.*, 2012; *Zhou et al.*, 2015], and EMIC waves [*Anderson and Hamilton*, 1993; *Zhang et al.*, 2012]. Here we also show in Figure 2i a wave magnetic field power spectrogram: the overplotted black dashed line is the hydrogen gyrofrequency, the black solid line is the helium gyrofrequency, and the black dash-dotted line is the oxygen gyrofrequency. Broadband waves were observed immediately after the shock arrival with wave normal angles in the quasi-parallel direction and ellipticity about zero (not shown here). Although these waves have frequencies in the EMIC wave range, these waves might be different from typical EMIC waves, which often have a clear banded structure. Moreover, this EMIC wave activity is closely related to

Figure 2. Summary plot of the 2 October 2013 IP shock event. (a) IMF B_z in GSM coordinates, (b) solar wind dynamic pressure, (c) AE index, and (d) SYM-H index. (e–m) The Van Allen Probe B observations 30 min prior to and 30 min after the shock arrival. Solar wind parameters and geomagnetic indices obtained from OMNI data are plotted in Figures 2a–2d 1 h prior to and 1 h after the shock arrival. The electromagnetic fields and $\mathbf{E} \times \mathbf{B}$ drift velocity in a mean local field-aligned coordinate system are plotted in Figures 2e–2h. The parallel direction $\mathbf{p}$ is determined by 20 min sliding averaged magnetic field, the azimuthal direction $\mathbf{a}$ is parallel to the cross product of the $\mathbf{p}$ and the spacecraft position vector, and the $\mathbf{r}$ component completes the triad. Figure 2i shows the EMIC wave spectrum as functions of frequency and UT. The overlapped dashed, solid, and dash-dotted lines are the gyrofrequency of hydrogen, helium, and oxygen, respectively. Figures 2j–2m are the spin-averaged energy flux of electron, hydrogen, helium, and oxygen as functions of energy and UT obtained from the HOPE instrument onboard Van Allen Probe B, respectively. The overlapped white line is azimuthal component of the electric field in a local field-aligned coordinates.

the low-energy ion flux enhancement associated with the sudden compression of the magnetosphere. The enhancement of low-energy (<100 eV) ion fluxes could contribute to an increase in cold plasma density, which would lower the resonant proton energy. However, they are unlikely to be the source population of generating EMIC waves, since the minimum ion resonant energy for EMIC wave generation is typically above 1 keV [e.g., *Horne and Thorne*, 1993]. Previous studies have shown that anisotropic ion distributions can generate EMIC waves [e.g., *Horne and Thorne*, 1993], and the strong temperature anisotropy in association
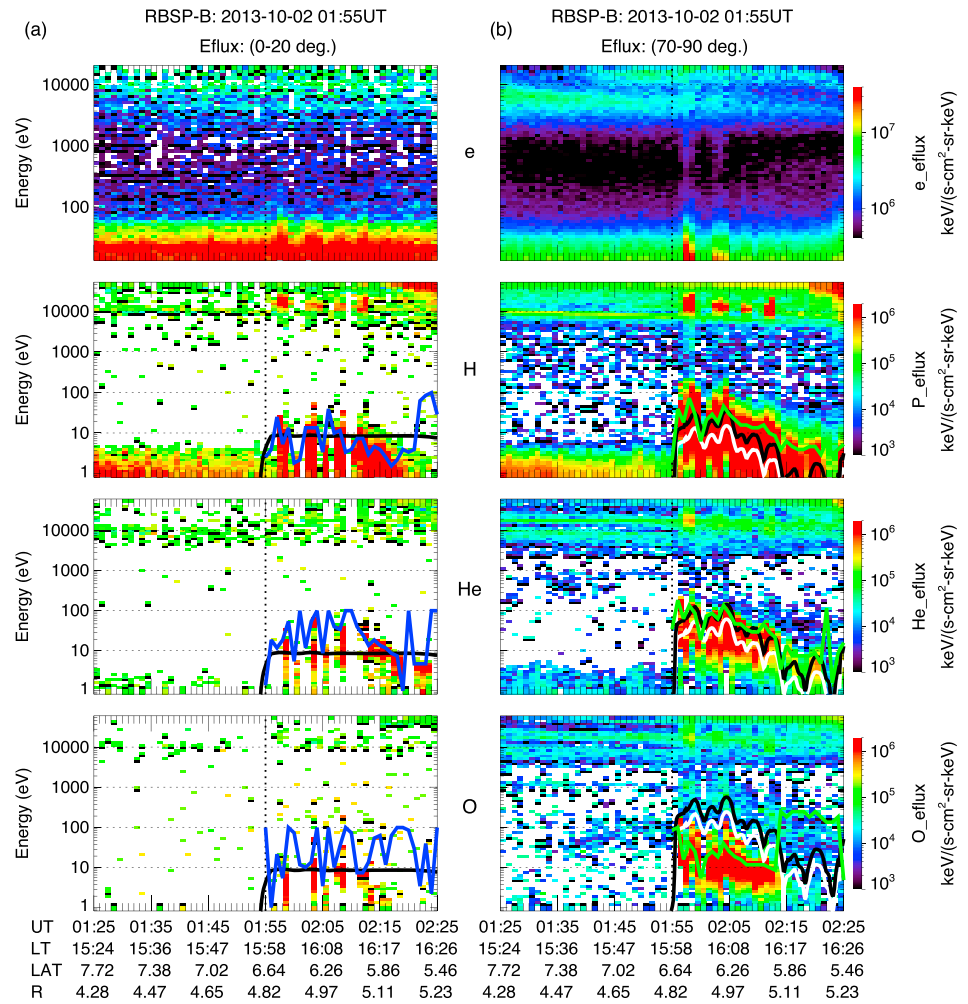
Figure 3. The energy flux of different species (e^-, H^+, He^+, and O^+ from top to bottom) observed by Van Allen Probe B within 30 min of the 2 October 2013 IP shock arrival (01:55 UT) in (a) parallel direction (0–20° pitch angle) and (b) perpendicular directions (70–90° pitch angle) as functions of energy and UT. The pitch angles from 90° to 180° are mirrored and added to 0°–90° range. The overplotted black line in Figure 3a is the energy gain due to magnetic field compression. The overplotted while line in Figure 3b is the energy gain corresponding to $\mathbf{E} \times \mathbf{B}$ drift, and the black line is the energy gain obtained from both $\mathbf{E} \times \mathbf{B}$ drift and the betatron acceleration/deceleration as particle drift toward to satellite position. The blue lines in Figure 3a and green lines in Figure 3b are the corresponding energy of e-folding of maximum low-energy ion fluxes, which represent the significant flux energy level after the shock arrival.

with enhanced fluxes of >1 keV ions was developed in this event as shown in details in Figure 3, which could provide a source of free energy for EMIC wave excitation after the shock arrival.

The low-energy (<100 eV) fluxes of electron (e^-), hydrogen (H^+), helium (He^+), and oxygen (O^+) dramatically increased, and the enhancement lasted more than 20 min after the IP shock arrival, as shown in Figures 2j–2m. The overplotted white line is the azimuthal component of electric field E_a. The low-energy electron flux and the ~10 keV ion fluxes were correlated well with the ULF oscillation of the electric field. This observation leads to the question: where did the low-energy ions come from and what mechanisms were responsible for the fast acceleration of the low-energy ions? In Figure 3, we demonstrate the possible source and acceleration mechanisms in detail.

Figures 3a and 3b show the energy flux of e^-, H^+, He^+, and O^+ in the parallel (0–20° pitch angle) and perpendicular (70–90° pitch angle) directions, respectively. Here pitch angle data at 90–180° were mirrored and added to 0–90° data (the pitch angle distribution is fairly symmetric in this case). As shown, the low-energy ion fluxes increased dramatically right after the shock arrival and lasted more than 20 min in both parallel and
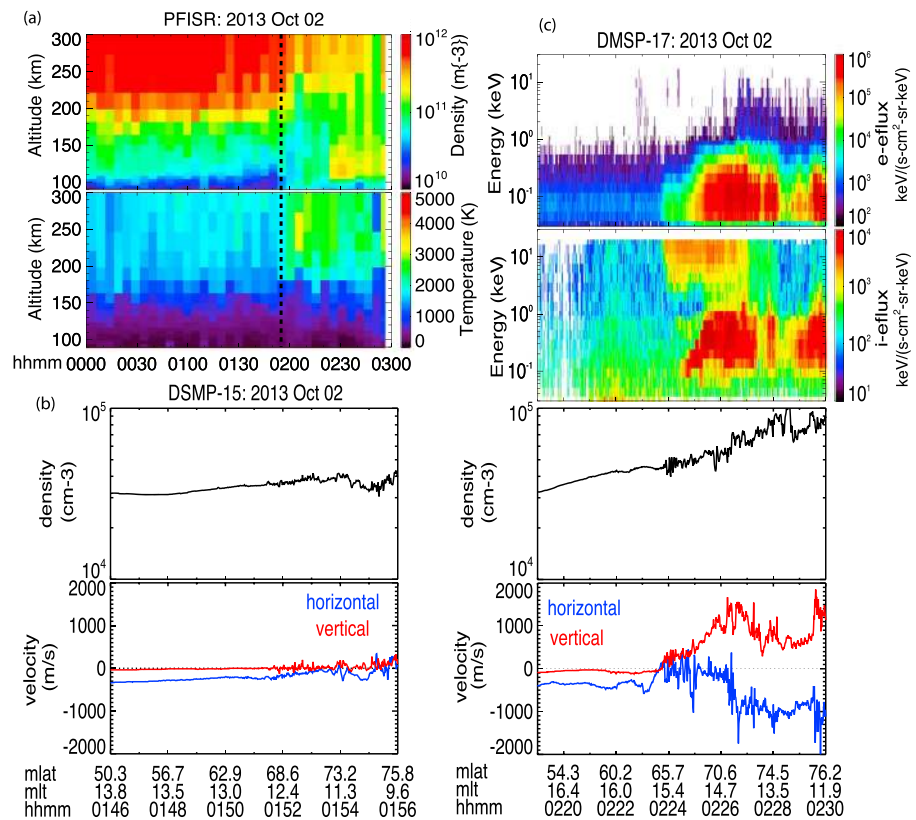
Figure 4. (a) The ground-based PFISR radar observations of plasma density and temperature variations as functions of altitude and UT prior and after 2 October 2013 shock arrival. The vertical dashed line marks the shock arrival time. (b) The plasma density and velocity variations observed by DSMP 15 before the IP shock arrival. The red line indicates the vertical flow velocity, while the blue line indicates the cross-track horizontal velocity. Positive values of the vertical flow mean upward flow, while negative values mean downward flow. (c) The energy fluxes of electron and proton and plasma density and velocities observed by DMSP 17 after the shock arrival. The format of flow velocity is the same as DMSP 15.

perpendicular directions with a larger enhancement in the perpendicular direction. Meanwhile, the energy gain of the approximately tens of keV ions was also preferentially in the perpendicular direction. The anisotropic distribution of tens of keV ions maybe responsible for the excitation of the broadband EIMC wave observed in Figure 2i.

The overplotted black solid lines in the bottom three panels of Figure 3a are the energy gain calculated from equation (3) due to the adiabatic acceleration in the parallel direction, while the blue lines are the corresponding energy of e-folding of maximum low-energy ion fluxes, which represent the significant flux energy level after the shock arrival. Here we have used the dipole magnetic field model to represent the quiet time magnetic field configuration in the inner magnetosphere and assumed that $a = 2.5/3$ is constant after the shock arrival in equation (3). Note that we modified the dipole magnetic field intensity at the Earth's surface to match the observed magnetic field before the shock arrival. From the results shown in Figure 3a, although the black line does not perfectly match the energy variation (as shown by the blue lines) for each species (H^+, He^+, and O^+) (if the value of α were assumed to be a function of time, the result would be better), it implies that the compression of the magnetic field could account for the energy gain in the parallel direction. In addition, it is possible that the ionospheric outflow could also contribute to the energy flux enhancement during the later time as we will discuss in detail in Figure 4.

The white lines overplotted in the bottom three panels of Figure 3b are the energy derived from equation (1), where the final energy appears to have a mass dependence. Here we have assumed the initial energy $W_{\perp,i} = 0$, which may bring some artificial errors since we indeed observed some low-energy (<5 eV) fluxes of H^+ and He^+ before the shock arrival. The overplotted green lines are the corresponding energy levels of e-folding of

the peak low-energy ion fluxes, which represent the significant flux energy levels. The energy gain for O^+ is above the significant flux energy level represented by the green line, while the energy gains for H^+ and He^+ are lower than the significant energy level observed by Van Allen Probe B. This indicates that the H^+ and He^+ ions require additional acceleration rather than the $\mathbf{E} \times \mathbf{B}$ drift alone, while O^+ ions can be explained by the $\mathbf{E} \times \mathbf{B}$ drift. If the particles observed by the Van Allen Probes traveled from other radial distances, the particles would also experience betatron acceleration or deceleration depending on satellite location and particle drift direction.

According to equation (2), we have calculated the energy change due to betatron acceleration for H^+, He^+, and O^+ after the IP shock arrival. Here we obtained L_i by back-tracing the particle trajectory in the radial direction. B_i is obtained from the modified dipole field model, which is the same as the model we used for parallel energy calculation. Here we have used the dipole magnetic field model to represent the quiet time magnetic field configuration in the inner magnetosphere. Note that we modified the dipole magnetic field intensity at the Earth's surface to match the observed magnetic field 30 min before the shock arrival. B_f is the observed magnetic field intensity, while $W_{\perp,i}$ is the particle perpendicular energy obtained from equation (1). We added the betatron acceleration to the $\mathbf{E} \times \mathbf{B}$ drift effect, and the results are plotted in black lines shown in Figure 3b. It is shown that the total energy gain calculated from $\mathbf{E} \times \mathbf{B}$ drift and betatron acceleration is fairly consistent with the observed energy increases (as shown by the green lines) for H^+ and He^+. The results indicate that the observed H^+ and He^+ particles mainly came from the ambient plasmasphere experiencing betatron acceleration during inward transport (the net time integral of velocity almost always pointed radially inward after the shock arrival), while the O^+ fraction around the H^+ and He^+ source location might be very small and O^+ originated in the plasmasphere just nearby the satellite location. These ion energy flux enhancements in perpendicular directions are caused by the induced electric field and/or betatron acceleration after the passage of IP shock.

Previous studies [e.g., *Fuselier et al.*, 2001] have shown that direct topside ionospheric heating could provide significant and nearly instantaneous ionospheric outflow in response to the passage of an IP shock. This indicates that the ionosphere is a possible source that contributes to magnetospheric parallel flux enhancement. In order to investigate whether ionospheric outflow contributes to the fast acceleration in the parallel direction for this shock event, we examined coincident ionospheric and ground-based observations. Figure 4a shows the PFISR radar observation of plasma density and temperature as a function of altitude from 00:00 to 03:00 UT on 2 October 2013. During this time period, the PFISR radar is very close to the footprint of Van Allen Probe B that is around 65° in geomagnetic latitude based on the TS01 model [*Tsyganenko*, 2002a, 2002b]. The vertical dashed line marks the shock arrival time at 01:55 UT. Observations show that the plasma density increased at low altitudes ($<$150 km) and the temperature increased from less than 2000 to ~3000 K over the altitudes of 200–300 km after the shock arrival (01:55 UT), indicating that higher-energy particles precipitated deeper into the ionosphere and heated the ionosphere. Figures 4b and 4c show the DMSP 15 and 17 observations prior to and after the shock arrival. Here we select DMSP 15 and 17 because their orbits were quite near the footprint of Van Allen Probe B during the time interval. Figure 4b shows DMSP 15 observations of plasma density and velocity prior to the shock arrival. Note that particle data were not available from this satellite. The red line indicates vertical flow velocity, while the blue line indicates the cross-track horizontal velocity. Positive values of vertical flow mean upward flow, while negative values mean downward flow. The density and velocities were almost flat along the orbit. Figure 4c shows DMSP 17 observations of energy fluxes of electron and ions, density, and flow velocities after the shock arrival. Around the Van Allen Probe B footprint (65° in latitude), the plasma density and the vertical flow velocity were higher compared with those shown in Figure 4b. Meanwhile, there were ring current ions and low-energy plasma precipitations indicated by the flux increases. From the ionospheric and ground-based observation, we conclude that there was stronger precipitation and ionospheric upflow after the shock arrival. Although we do not have measurements above the DMSP altitudes, part of the upflowing ions are expected to accelerate further and flow out to the magnetosphere.

Although the upflows were observed after the shock arrival, it should take some time for these particles to be transported from the ionosphere along the field line to the observational point of Van Allen Probes B. Comparing the ions of different species with the same energy, H^+ travels fastest while O^+ travels slowest. We have calculated that 10–100 eV H^+ (He^+ and O^+) ions take about 4.5–14 min (9–28 min and 18–56 min),
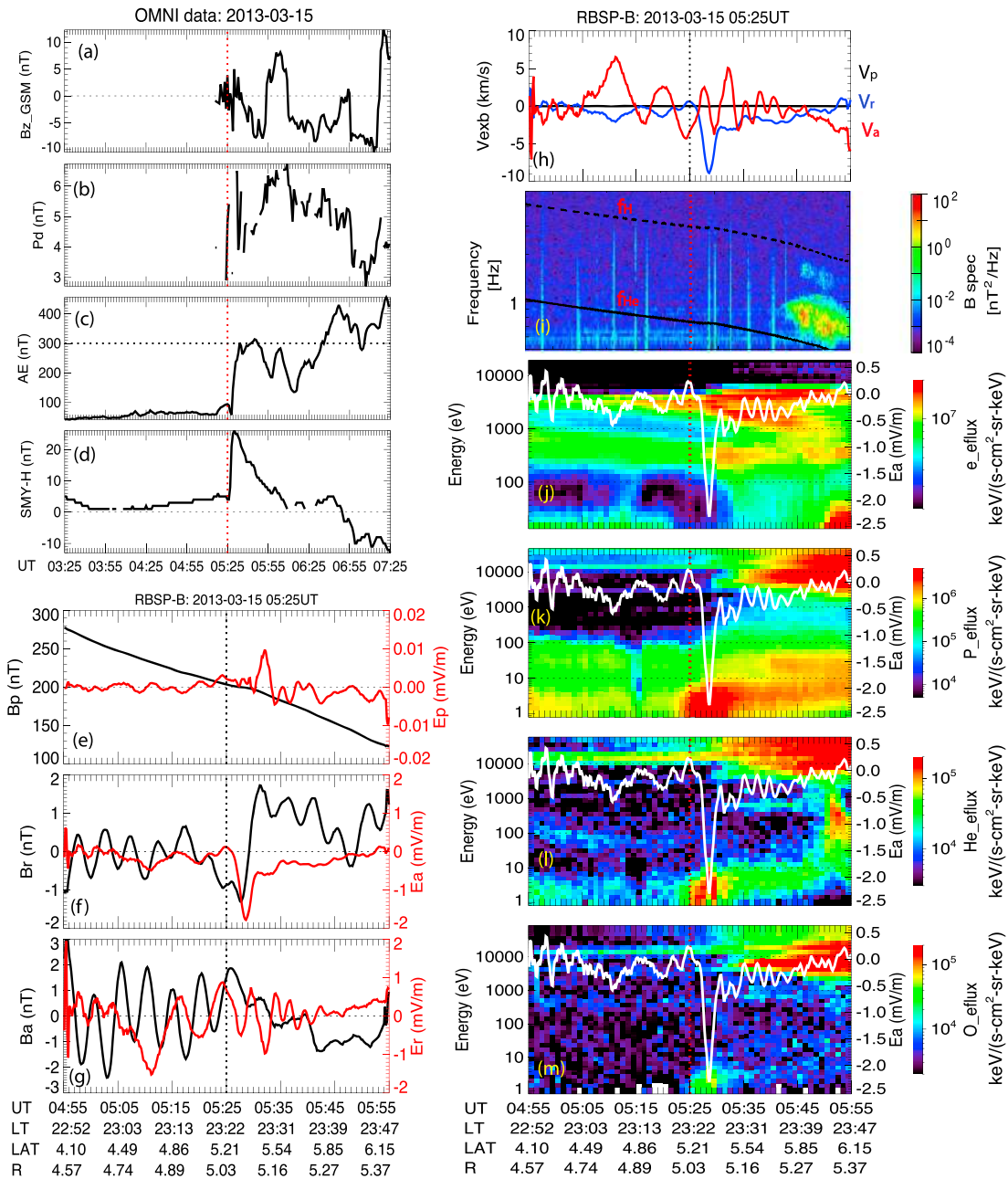
Figure 5. Summary plot of the 15 March 2013 IP shock event. The format is same as in Figure 2.

respectively, to travel from the ionosphere to L = 5 at the magnetic equator, and higher-energy particles travel faster. However, from the results shown in Figure 3a, there was no apparent time delay among different ion species. Moreover, the response time to the IP shock was less than 4 min for all different ion species. Therefore, the ionospheric outflow is inconsistent with the observed time delay and is unlikely to contribute to the initial accelerated cold plasma caused by the passage of IP shock, while it may contribute to the low-energy ion flux increase at later times (>5 min) after the shock arrival.

3.2. 15 March 2013 Shock Event

Figure 5 shows a summary plot of the 15 March 2013 IP shock event, which occurred at 05:25 UT and was indicated by the sudden increase of solar wind dynamic pressure and *SYM-H*, in the same format as Figure 2. After the shock arrival, the IMF B_z (Figure 5a) gradually decreased from 0 to about −8 nT in
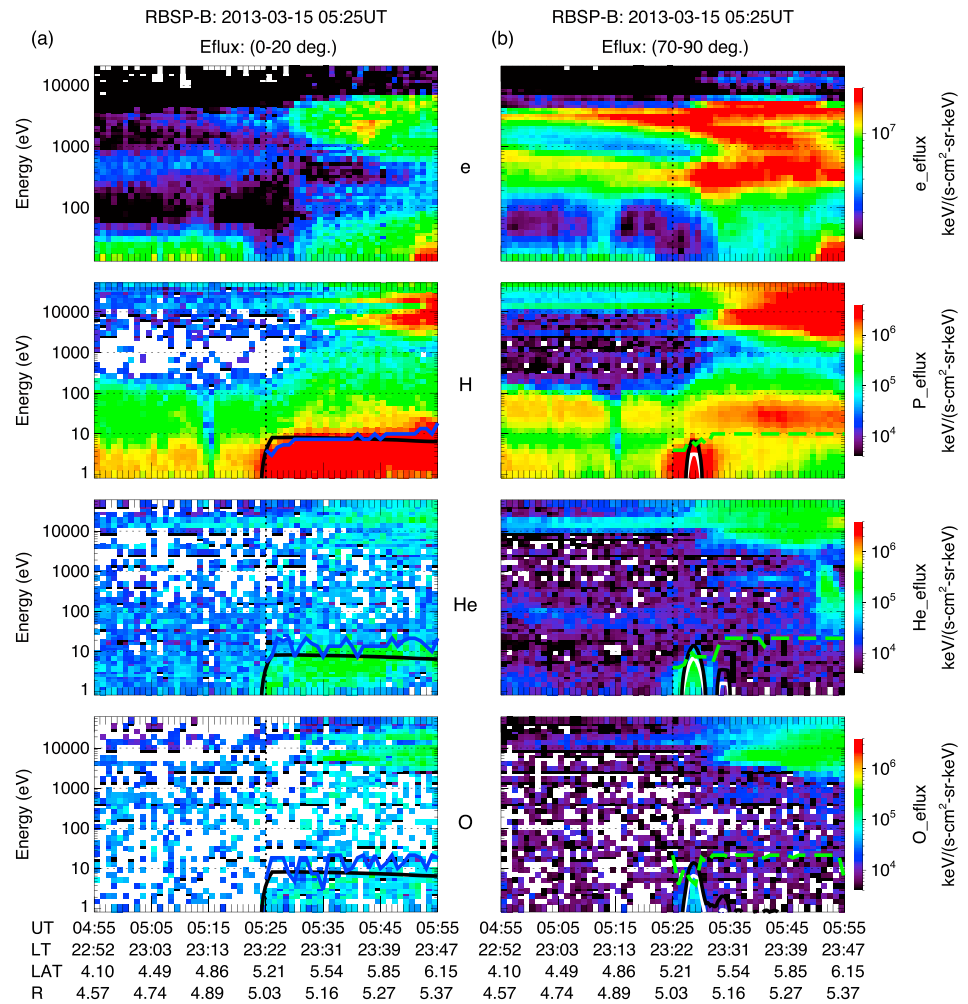
Figure 6. The energy fluxes of different species (e⁻, H⁺, He⁺, and O⁺ from top to bottom) observed by Van Allen Probe B within 30 min of the IP shock arrival (05:25 UT) in (a) parallel direction (0–20° pitch angle) and (b) perpendicular direction (70–90° pitch angle) as functions of energy and UT. The format is the same as in Figure 3.

10 min. The solar wind dynamic pressure (Figure 5b) increased from 3 to 6 nPa. Meanwhile, the *AE* index (Figure 5c) increased from 100 nT to 300 nT. In addition, the *SYM-H* index (Figure 5d) abruptly jumped from about 5 to 25 nT. This is a moderate IP shock event compared with the first event.

Van Allen Probe B was located around midnight and provided the electromagnetic field measurements and the $\mathbf{E} \times \mathbf{B}$ drift velocities in a mean local field-aligned coordinate system as shown in Figures 5e–5h. In contrast to the first case, the electric field intensity was much smaller with a maximum amplitude of ~2 mV/m and showed only one electric pulse of ~5 min in E_a component induced by the passage of the IP shock, resulting in smaller $\mathbf{E} \times \mathbf{B}$ velocity in Figure 5h. Clear hydrogen band EMIC waves were observed 15 min after the shock arrival. The wave intensification was very likely triggered by the injection of tens of keV ions as shown in Figures 5k–5m. Meanwhile, the low-energy (<10 eV) ion fluxes of different species dramatically increased immediately after the IP shock arrival.

In order to identify the source of the cold ions and the acceleration mechanisms, Figure 6 demonstrates the energy flux variations in the parallel and perpendicular directions for e⁻, H⁺, He⁺, and O⁺ as a function of energy within 30 min of the shock arrival. Here pitch angle data at 90–180° were mirrored and added to 0–90° data (the pitch angle distribution shows a slight asymmetry in this case). The overplotted solid black lines and white lines in the bottom three panels of Figure 6 represent the energy gains from different acceleration mechanisms in the same format as Figure 3, and the overplotted blue lines and dashed green
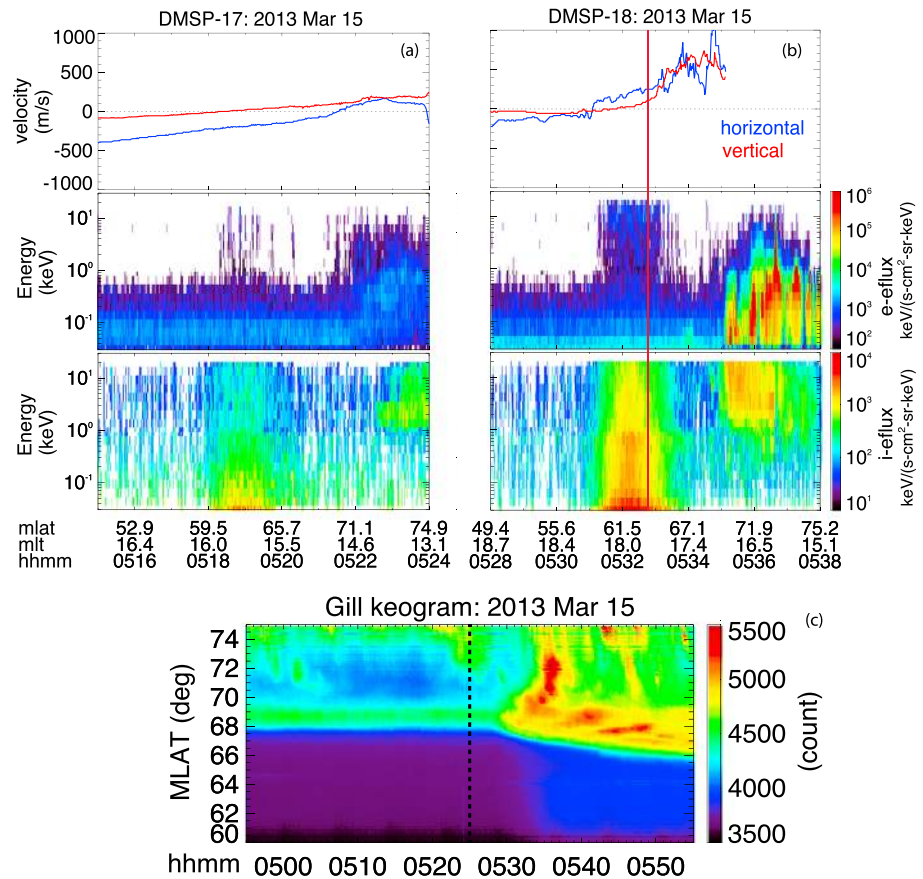
Figure 7. (a) The ionospheric flow velocity and energy flux of electron and proton observed by DMSP 17 prior to the IP shock arrival. The red line indicates vertical flow velocity, while the blue line indicates the cross-track horizontal velocity. Positive values of vertical flow mean upward flow, while negative values mean downward flow. (b) The ionospheric flow velocities and energy fluxes of electron and proton observed by DMSP 18 after the IP shock arrival. The format is the same as Figure 7a; the red vertical line marks the time when the vertical flow velocity increases. (c) The keogram obtained from the THEMIS ASI Gill station prior to and after the IP shock arrival. The vertical dashed line marks the shock arrival time.

lines are the corresponding energy level of e-folding of the peak low-energy ion fluxes. Here we have used dashed green lines instead of solid green lines to emphasis that the comparison of energy gain in perpendicular direction in Figure 6b is only for the first 5 min when there is induced electric field. In contrast to the first case, the energy level of flux increases was only up to 10 eV as shown by the blue and green lines, which was probably because of the weaker IP shock impinging. Meanwhile, the parallel flux increase lasted more than 30 min, while the perpendicular energy gain only occurred at the first 5 min after the shock arrival. The low-energy parallel flux increases could be caused by the magnetic field compression as shown in Figure 6a, indicated by the fairly good match of the black lines which were obtained based on the calculation from equation (3) with the blue lines (the significant flux energy level). However, the perpendicular flux increases were mainly due to the induced electric field (as shown in Figure 5m with the overplotted E_a component) acceleration as indicated by the white and black lines shown in Figure 6b. Comparing the green lines with those white and black lines in Figure 6b during the period when there is induced electric field, it is shown that the green lines are above the white lines for both H^+ and He^+, while the green line falls below the white line for O^+, indicating that both the $\mathbf{E} \times \mathbf{B}$ drift and betatron accelerations play important roles in energizing H^+ and He^+, while O^+ ions can be explained solely by the $\mathbf{E} \times \mathbf{B}$ drift.

Figure 7 shows the coincident ionospheric and ground-based observations in response to the IP shock during the case 2. Figures 7a and 7b show the DMSP 17 and DMSP 18 observations of plasma velocities and energy fluxes of electrons and ions prior to and after the IP shock arrival, respectively. Here we select DMSP 17 and 18 because their orbits are quite close to the footprint of Van Allen Probe B during the time interval. The vertical

flow velocity was about 0, and there was almost no precipitation prior to the IP shock arrival in Figure 7a. However, the vertical flow velocity increased and the ring current particle precipitations were observed after the shock arrival, as shown in Figure 7b. Figure 7c shows the THEMIS ASI keogram at Gill station, which was very close to the magnetic local time of Van Allen Probes B (~64° in latitude) within 30 min of the IP shock arrival. The vertical dashed line marks the shock arrival time at 05:25 UT. Before the shock arrival, there was weak diffuse aurora around the latitude over 68–69.5°. The diffuse aurora intensified and moved to lower latitudes 4 min after the shock arrival. The ionospheric and ground-based signatures indicate that there was stronger precipitation and ionospheric outflow triggered by the IP shock. As discussed previously, these ionospheric outflows were unlikely to contribute to the initial acceleration of low-energy ions immediately after the shock arrival observed by Van Allen Probe B, due to the several to tens of minutes of travel time from the ionosphere to the satellite location. However, these ionospheric outflows could contribute to later time flux increases [*Fuselier et al.*, 2001], which lasted at least until 05:55 UT, as shown in Figure 6a.

4. Discussion and Summary

In order to understand where the source of enhanced low-energy plasma (<100 eV) is located in the inner magnetosphere during IP shock events and what mechanisms are responsible for the fast acceleration caused by the impact of IP shocks, we have examined two shock cases with different plasma properties that occurred when the favorable ionospheric and ground observations were available and Van Allen Probes were located near the magnetic equator in the afternoon and midnight sectors with good conjunction with ionospheric and ground observations. We have performed detailed analysis of low-energy ion fluxes enhancement due the impact of IP shocks in parallel and perpendicular directions and compared our observations with the simple particle motion calculations. We have found that the rapid response of low-energy ions is due to drifts of plasmaspheric population by the enhanced electric field associated with the impinging of IP shocks as well as the adiabatic accelerations in both the parallel and perpendicular directions. In addition, the initially enhanced low-energy plasma could come from the ambient plasmasphere, whereas the topside ionosphere could contribute to the low-energy ion flux increase at later time (>5 min) after the shock arrival.

Previous studies [e.g., *Zong et al.*, 2012; *Zhang et al.*, 2012] have suggested that the $\mathbf{E} \times \mathbf{B}$ drift is responsible for the tens of eV ion flux enhancements associated with the IP shock impact. However, from our investigation, the low-energy ion acceleration cannot be fully explained by the $\mathbf{E} \times \mathbf{B}$ drift, and adiabatic accelerations also play important roles. *Zhang et al.* [2012] have concluded that those enhanced low-energy ions are the plasmaspheric plume populations, while we have demonstrated that the ionosphere can be another source of enhanced low-energy plasma besides the plasmaspheric populations.

Based on our careful investigation of favorable observations and theoretical calculations, we have the following main findings:

1. Associated with the shock arrival, the electromagnetic fields intensify, and parallel and perpendicular energy fluxes of low-energy ions, including H^+, He^+, and O^+, show a dramatic enhancement. In the duskside case, broadband waves in the EMIC wave frequency range were excited in response to the IP shock, while in the nightside case the EMIC wave is most likely generated by the injections of tens of keV particles triggered by the impact of IP shock.
2. Both parallel and perpendicular low-energy ion fluxes increase immediately and last >20 min after the shock arrival for 2 October 2013 shock event with a larger enhancement in the perpendicular direction. In the 15 March 2013 shock event, while the perpendicular population flux increase only lasts 5 min, the parallel flux increase lasts more than 30 min after the shock arrival.
3. The particle precipitation and ionospheric outflows are observed from the ionospheric and ground-based observation associated with the shock arrival.
4. The fast acceleration of perpendicular energy flux at low-energy range is mainly caused by the $\mathbf{E} \times \mathbf{B}$ drift and betatron acceleration of the low-energy particles that drift toward the Van Allen Probes from the ambient plasmasphere.
5. The initial increase of the parallel direction energy flux of low-energy ions after the IP shock arrival is most likely related to the parallel adiabatic acceleration in response to the impact of the IP shock. The cold ions accelerated some time after the shock arrival could come from the ionospheric outflow that is generated by the direct topside ionospheric heating due to the moderate precipitation caused by the passage of IP shock.

In this paper, we have demonstrated that the initially enhanced cold plasma (<100 eV) energy flux triggered by the impact of IP shock is the plasmaspheric population. The rapidly accelerated low-energy ions are mainly caused by the induced electric field as well as the compression of the magnetic field due to the impact of the IP shock. However, there are still unsolved puzzles that deserve further investigation. For example, how much the parallel electric field contributes to the low-energy particle acceleration in the parallel direction although it is usually assumed quite small based on previous studies [e.g., *Zong et al.*, 2012]. It is also interesting to find the modulation of the low-energy ion fluxes during the 2 October 2013 shock event, which we hypothesize as being related to drift-bouncing resonances of the ULF waves induced by the IP shock [*Dai et al.*, 2013; *Claudepierre et al.*, 2013]. It is also important to investigate the energy budget issues, such as the energy deposited from the inner magnetosphere to the ionosphere, and the energy range of the inner magnetosphere particles which are scattered and precipitated to the ionosphere and generate aurora. Besides the $\mathbf{E} \times \mathbf{B}$ drift and adiabatic acceleration, what are the other mechanisms responsible to the electron acceleration? Addressing the above issues would contribute to a better understanding of the responses of the inner magnetosphere to IP shock impacts.

References

Anderson, B. J., and D. C. Hamilton (1993), Electromagnetic ion cyclotron waves stimulated by modest magnetospheric compressions, *J. Geophys. Res.*, *98*(A7), 11,369–11,382, doi:10.1029/93JA00605.

André, M., and A. Yau (1997), Theories and observations of ion energization and outflow in the high latitude magnetosphere, *Space Sci. Rev.*, *80*(1-2), 27–48, doi:10.1023/A:1004921619885.

André, M., and C. M. Cully (2012), Low-energy ions: A previously hidden solar system particle population, *Geophys. Res. Lett.*, *39*, L03101, doi:10.1029/2011GL050242.

Claudepierre, S. G., et al. (2013), Van Allen Probes observation of drift-resonance between poloidal mode ultra-low frequency waves and 60 keV electrons, *Geophys. Res. Lett.*, *40*, 4491–4497, doi:10.1002/grl.50901.

Dai, L., et al. (2013), Excitation of Poloidal standing Alfven waves through the drift resonant wave-particle interaction, *Geophys. Res. Lett.*, *40*, 4127–4132, doi:10.1002/grl.50800.

Foster, J. C., J. R. Wygant, M. K. Hudson, A. J. Boyd, D. N. Baker, P. J. Erickson, and H. E. Spence (2015), Shock-induced prompt relativistic electron acceleration in the inner magnetosphere, *J. Geophys. Res. Space Physics*, *120*, 1661–1674, doi:10.1002/2014JA020642.

Fu, H. S., J. B. Cao, F. S. Mozer, H. Y. Lu, and B. Yang (2012), Chorus intensification in response to interplanetary shock, *J. Geophys. Res.*, *117*, A01203, doi:10.1029/2011JA016913.

Funsten, H. O., et al. (2013), Helium, Oxygen, Proton, and Electron (HOPE) Mass Spectrometer for the Radiation Belt Storm Probes Mission, *Space Sci. Rev.*, *179*(1), 423–484, doi:10.1007/s11214-013-9968-7.

Fuselier, S. A., et al. (2001), Ion outflow observed by IMAGE: Implications for source regions and heating mechanisms, *Geophys. Res. Lett.*, *28*(6), 1163–1166, doi:10.1029/2000GL012450.

Gombosi, T. I., and T. L. Killeen (1987), Effects of thermospheric motions on the polar wind: A time-dependent numerical study, *J. Geophys. Res.*, *92*(A5), 4725–4729, doi:10.1029/JA092iA05p04725.

Hardy, D. A., L. K. Schmitt, M. S. Gussenhoven, F. J. Marshall, H. C. Yeh, T. L. Shumaker, A. Hube, and J. Pantazis (1984), Precipitating electron and ion detectors (SSJ/4) for the block 5D/flights 6–10 DMSP satellites: Calibration and data presentationRep AFGL-TR-84-0317Air Force Geophys. Lab., Hanscom Air Force Base, Mass.

Heelis, R. A. (2006), Post-launch support for DMSP SSIES sensors (No. 630940) Texas Univ. at Dallas Richardson.

Heelis, R. A., G. J. Bailey, R. Sellek, R. J. Moffett, and B. Jenkins (1993), Field-aligned drifts in subauroral ion drift events, *J. Geophys. Res.*, *98*(A12), 21,493–21,499, doi:10.1029/93JA02209.

Horne, R. B., and R. M. Thorne (1993), On the preferred source location for the convective amplification of ion cyclotron waves, *J. Geophys. Res.*, *98*(A6), 9233–9247, doi:10.1029/92JA02972.

Horwitz, J. L., and T. E. Moore (1997), Four contemporary issues concerning ionospheric plasma flow to the magnetosphere, in *Transport Across the Boundaries of the Magnetosphere*, pp. 49–76, Springer, Netherlands.

Iyemori, T. (1990), Storm-time magnetospheric currents inferred from mid-latitude geomagnetic field variations, *J. Geomagn. Geoelectr.*, *42*, 1249–1265, doi:10.5636/jgg.42.1249.

Iyemori, T., and D. R. K. Rao (1996), Decay of the *Dst* field of geomagnetic disturbance after substorm onset and its implication to storm-substorm relation, *Ann. Geophys.*, *14*, 608–618, doi:10.1007/s00585-996-0608-3.

Keika, K., et al. (2008), Response of the inner magnetosphere and the plasma sheet to a sudden impulse, *J. Geophys. Res.*, *113*, A07S35, doi:10.1029/2007JA012763.

Keika, K., L. M. Kistler, and P. C. Brandt (2013), Energization of O^+ ions in the Earth's inner magnetosphere and the effects on ring current buildup: A review of previous observations and possible mechanisms, *J. Geophys. Res. Space Physics*, *118*, 4441–4464, doi:10.1002/jgra.50371.

Kepko, L., and H. E. Spence (2003), Observations of discrete, global magnetospheric oscillations directly driven by solar wind density variations, *J. Geophys. Res.*, *108*(A6), 1257, doi:10.1029/2002JA009676.

Kletzing, C. A., et al. (2013), The Electric and Magnetic Field Instrument Suit and Integrated Science (EMFISIS) on RBSP, *Space Sci. Rev.*, *179*, 127–181, doi:10.1007/s11214-013-9993-6.

Li, X., D. N. Baker, S. Elkington, M. Temerin, G. D. Reeves, R. D. Belian, J. B. Blake, H. J. Singer, W. Peria, and G. Parks (2003), Energetic particle injections in the inner magnetosphere as a response to an interplanetary shock, *J. Atmos. Sol. Terr. Phys.*, *65*, 233–244, doi:10.1016/S1364-6826(02)00286-9.

Liou, K., P. T. Newell, C.-I. Meng, C.-C. Wu, and R. P. Lepping (2003), Investigation of external triggering of substorms with Polar ultraviolet imager observations, *J. Geophys. Res.*, *108*(A10), 1364, doi:10.1029/2003JA009984.

Mauk, B. H., N. J. Fox, S. G. Kanekal, R. L. Kessel, D. G. Sibeck, and A. Ukhorskiy (2013), Science objectives and rationale for the Radiation Belt Storm Probes Mission, *Space Sci. Rev.*, *179*(1), 3–27, doi:10.1007/s11214-012-9908-y.

Mende, S. B., S. E. Harris, H. U. Frey, V. Angelopoulos, C. T. Russell, E. Donovan, B. Jackel, M. Greffen, and L. M. Peticolas (2008), The THEMIS array of ground-based observatories for the study of auroral substorms, *Space Sci. Rev.*, *141*, 357–387, doi:10.1007/s11214-008-9380-x.

Olson, J. V., and L. C. Lee (1983), Pc1 wave generation by sudden impulses, *Planet. Space Sci.*, *31*(3), 295–302, doi:10.1016/0032-0633(83)90079-X.

Parks, C. (1975), Whistler observations during a magnetospheric sudden impulse, *J. Geophys. Res.*, *80*(34), 4738–4740, doi:10.1029/JA080i034p04738.

Shue, J. H., et al. (1998), Magnetopause location under extreme solar wind conditions, *J. Geophys. Res.*, *103*(A8), 17,691–17,700, doi:10.1029/98JA01103.

Southwood, D. J., and M. G. Kivelson (1975), An approximate analytic description of plasma bulk parameters and pitch angle anisotropy under adiabatic flow in a dipolar maenetosoheric field, *J. Geophys. Res.*, *80*, 2069–2073, doi:10.1029/JA080i016p02069.

Spence, H. E., et al. (2013), Science goals and overview of the energetic particle, composition, and thermal plasma (ECT) suite on NASA's Radiation Belt Storm Probes (RBSP) mission, *Space Sci. Rev.*, *179*(1–4), 311–336, doi:10.1007/s11214-013-0007-5.

Thomsen, M. F., J. E. Borovsky, D. J. McComas, R. C. Elphic, and S. Maurice (1998), The magnetospheric response to the CME passage of January 10–11, 1997, as seen at geosynchronous orbit, *Geophys. Res. Lett.*, *25*(14), 2545–2548, doi:10.1029/98GL00514.

Tsyganenko, N. A. (2002a), A model of the near magnetosphere with a dawn-dusk asymmetry: 1. Mathematical structure, *J. Geophys. Res.*, *107*(A8), 1179, doi:10.1029/2001JA000219.

Tsyganenko, N. A. (2002b), A model of the near magnetosphere with a dawn-dusk asymmetry: 2. Parameterization and fitting to observations, *J. Geophys. Res.*, *107*(A8), 1176, doi:10.1029/2001JA000220.

Wang, C., J. B. Liu, H. Li, Z. H. Huang, J. D. Richardson, and J. R. Kan (2009), Geospace magnetic field responses to interplanetary shocks, *J. Geophys. Res.*, *114*, A05211, doi:10.1029/2008JA013794.

Wygant, J. R., et al. (2013), The electric field and waves instruments on the radiation belt storm probes mission, *Space Sci. Rev.*, *179*(1-4), 183–220, doi:10.1007/s11214-013-0013-7.

Yue, C., and Q. Zong (2011b), Solar wind parameters and geomagnetic indices for four different interplanetary shock/ICME structures, *J. Geophys. Res.*, *116*, A12201, doi:10.1029/2011JA017013.

Yue, C., Q.-G. Zong, and Y. F. Wang (2009), Response of the magnetic field and plasmas at the geosynchronous orbit to interplanetary shock, *Chin. Sci. Bull.*, *54*, 4241–4252, doi:10.1007/s11434-009-0649-6.

Yue, C., Q.-G. Zong, H. Zhang, Y. F. Wang, C. J. Yuan, Z. Y. Pu, S. Y. Fu, A. T. Y. Lui, B. Yang, and C. R. Wang (2010), Geomagnetic activities triggered by interplanetary shocks, *J. Geophys. Res.*, *115*, A00I05, doi:10.1029/2010JA015356.

Yue, C., Q. Zong, Y. Wang, I. I. Vogiatzis, Z. Pu, S. Fu, and Q. Shi (2011a), Inner magnetosphere plasma characteristics in response to interplanetary shock impacts, *J. Geophys. Res.*, *116*, A11206, doi:10.1029/2011JA016736.

Yue, C., Y. Nishimura, L. R. Lyons, V. Angelopoulos, E. F. Donovan, Q. Shi, Z. Yao, and J. W. Bonnell (2013), Coordinated THEMIS spacecraft and all-sky imager observations of interplanetary shock effects on plasma sheet flow bursts, poleward boundary intensifications, and streamers, *J. Geophys. Res. Space Physics*, *118*, 3346–3356, doi:10.1002/jgra.50372.

Zhang, H., D. G. Sibeck, Q. G. Zong, J. P. McFadden, D. Larson, K. H. Glassmeier, and V. Angelopoulos (2012), Global magnetospheric response to an interplanetary shock: THEMIS observations, *Ann. Geophys.*, *30*(2), 379–387, doi:10.5194/angeo-30-379-2012.

Zhou, C., et al. (2015), Excitation of dayside chorus waves due to magnetic field line compression in response to interplanetary shocks, *J. Geophys. Res. Space Physics*, *120*, 8327–8338, doi:10.1002/2015JA021530.

Zhou, X., and B. T. Tsurutani (2001), Interplanetary shock triggering of nightside geomagnetic activity: Substorms, pseudobreakups, and quiescent events, *J. Geophys. Res.*, *106*(A9), 18,957–18,967, doi:10.1029/2000JA003028.

Zong, Q., Y. Wang, C. Yuan, B. Yang, C. Wang, and X. Zhang (2011), Fast acceleration of "killer" electrons and energetic ions by interplanetary shock stimulated ULF waves in the inner magnetosphere, *Chin. Sci. Bull.*, *56*(12), 1188–1201, doi:10.1007/s11434-010-4308-8.

Zong, Q.-G., X.-Z. Zhou, Y. F. Wang, X. Li, P. Song, D. N. Baker, T. A. Fritz, P. W. Daly, M. Dunlop, and A. Pedersen (2009), Energetic electrons response to ULF waves induced by interplanetary shocks in the outer radiation belt, *J. Geophys. Res.*, *114*, A10204, doi:10.1029/2009JA014393.

Zong, Q.-G., Y. F. Wang, H. Zhang, S. Y. Fu, H. Zhang, C. R. Wang, C. J. Yuan, and I. Vogiatzis (2012), Fast acceleration of inner magnetospheric hydrogen and oxygen ions by shock induced ULF waves, *J. Geophys. Res.*, *117*, A11206, doi:10.1029/2012JA018024.